1.58 Tbps OAM Multiplexing Wireless Transmission With Wideband Butler Matrix for Sub-THz Band

Hirofumi Sasaki, *Member, IEEE*, Yasunori Yagi, *Member, IEEE*, Riichi Kudo, *Member, IEEE*, and Doohwan Lee, *Senior Member, IEEE*

***Abstract*— Mobile traffic growth requires the advancement of not only the wireless access networks but also their backhaul and fronthaul. Terabit-class wireless backhaul and fronthaul can be an alternative to optical fiber transmission and will be one of the key technologies to construct a more flexible and less expensive network infrastructure for sixth-generation mobile networks (6G). However, it is a challenge to provide an extremely high-capacity wireless link for point-to-point connection without spatial multiplexing gain obtained by the multi-path rich environment. We demonstrated the world's highest wireless transmission data rate of 1.58 Tbps in the sub-terahertz (sub-THz) band for 6G backhaul and fronthaul networks on the basis of the orbital angular momentum (OAM) multiplexing technology with a wideband Butler matrix. Terabit-class wireless transmission was achieved by designing a wideband 8 × 8 Butler matrix with two types of 3-dB couplers for the structure without crossover and differential phase shifters that give the desired phase difference over wide bandwidth. Our Butler matrix is capable of multiplexing eight OAM beams and show a high mode isolation of greater than 15 dB and low insertion loss of less than 1.5 dB from 135 to 170 GHz. We implemented the Butler matrices in our OAM multiplexing transmission system, in which the physical-layer data rate of 1.58 Tbps wireless transmission was confirmed with eight OAM modes and dual polarization using the 32 GHz bandwidth.**

***Index Terms*— Orbital angular momentum (OAM), sub-THz, Butler matrix, wireless backhaul, electromagnetic signal and information theory (ESIT).**

I. Introduction

WIRELESS communication supports daily activities, and the amount of traffic continues to grow. The proliferation of connected devices is expected to accelerate the creation of new services, which require higher capacities such as augmented/virtual reality (AR/VR) and high-definition video transmission. Discussions of the next generation of wireless networks, i.e., sixth-generation mobile networks (6G), have begun, with visions for a variety of services and requirements [1], [2], [3]. The transmission data rate of wireless networks that aggregate various wireless traffic is expected to reach the terabit-class [4], so the capacity of backhaul and fronthaul for the base stations in the networks must be enlarged accordingly. Various backhaul architectures with different technologies have been considered [5], [6], [7] and such high-capacity requirements will arise, particularly in point-to-point (P2P) connections between core networks and base stations or between base stations. While the optical backhaul and fronthaul links provide stable large capacity regardless of the climate condition, wireless connectivity is advantageous in terms of the hardware costs [6] and deployment flexibility. Therefore, we believe terabit-class wireless transmission can provide a breakthrough in flexible high-capacity network infrastructure for 6G by taking advantage of wireless connectivity. In such P2P links, the connection is typically line-of-sight (LoS) [5], and it is assumed that millimeter wave (mmWave) and sub-terahertz (sub-THz) bands will be used for high directivity and wide and contiguous bandwidth utilization. A wideband transmission in such a high-frequency band is also highly compatible with fiber optics technologies [8], [9], [10], in which dozens of GHz bandwidth is typically used, and a combination of these technologies was proposed for broadband real-time transmission and seamless connection of fiber optics and wireless radio networks.

Thus, assuming LoS P2P wireless communication in mmWave and sub-THz bands for backhaul and fronthaul connections, the transmission channel between antennas is fixed and stable, and the environment is not multipath-rich, so the spatial resources are limited compared with conventional wireless systems based on multiple-input multiple-output (MIMO). Therefore, more efficient spatial utilization and system design are expected in the new framework of electromagnetic signal and information theory, which takes into account more fundamental physical properties of electromagnetic (EM) waves including near-field behavior and arbitrary wavefronts such as holographic MIMO [11], reconfigurable intelligent surfaces [12], and time-space coding meta-surfaces [13], [14].

Orbital angular momentum (OAM) is a physical property of EM beams with spatial phase and amplitude distributions and the beams with different OAM modes are orthogonal to each other. OAM multiplexing transmission technology enables the transmission of multiple independent data streams via the

Manuscript received 1 April 2023; revised 14 August 2023; accepted 4 December 2023. Date of publication 23 April 2024; date of current version 29 May 2024. An earlier version of this paper was presented in part at the 2023 IEEE International Conference on Communications Workshops (ICC Workshops) [DOI: 10.1109/ICCWorkshops57953.2023.10283809]. *(Corresponding author: Hirofumi Sasaki.)*

The authors are with the NTT Network Innovation Laboratories, Nippon Telegraph and Telephone Corporation, Yokosuka, Kanagawa 239-0847, Japan (e-mail: hirofumi.sasaki@ntt.com; yasunori.yagi@ntt.com; riichi.kudo@ntt.com; doohwan.lee@ntt.com).

Color versions of one or more figures in this article are available at https://doi.org/10.1109/JSAC.2024.3389125.

Digital Object Identifier 10.1109/JSAC.2024.3389125

OAM beams. In OAM multiplexing transmission, the spatial multiplexing gain is obtained without multi-path propagation by increasing the number of available OAM modes even in an LoS environment. The spatial distribution, or wavefront, of the OAM beams is physically defined, so their generation and separation process can be fixed, which means low-cost passive analog devices can be used. It is especially important for the practical implementation of wideband high-capacity transmission using dozens of GHz bandwidth in the high-frequency band since the development of dedicated high-speed digital signal processing (DSP) devices for spatial multiplexing is very difficult and operational costs including power consumption are assumed to be large. If passive analog devices can take on all of the multiplexing processing, seamless connections to other optical networks [8], [9], [10] can be expected. Studies on the methods of OAM beams forming have been conducted such as on spiral phase plates [15], [16], holographic plates [17], meta-surfaces [18], and uniform circular arrays (UCAs) [19], [20], [21], and multiplexing transmission has also been demonstrated in both the optical and radio communication fields [20], [21], [22], [23]. Unlike other methods, the use of UCAs does not require coaxial beam synthesis using a beam combiner or similar device and enables simultaneous generation of OAM beams with a simple antenna configuration, so we consider it practical and suitable for radio communications. When using UCAs, the beamforming process is also fixed, i.e., discrete Fourier transform (DFT), and an analog circuit called a Butler matrix can be used [24]. There have been numerous reports on the design and implementation of Butler matrices in the field of analog beamforming technology [25] not only for OAM multiplexing [26]. We have conducted several UCA-based OAM multiplexing transmission experiments using Butler matrices in the 28 and 40 GHz bands with a maximum physical-layer data rate of 200 Gbps under 100 m [27], [28], [29], [30].

To achieve terabit-class wireless transmission for backhaul and fronthaul wireless networks, we focused on the sub-THz band, especially the D-band (110–170 GHz), considering both a wide and continuous bandwidth utilization of a few dozen of GHz and the availability of various practical radio frequency (RF) devices. We developed a Butler matrix in the sub-THz band and investigated OAM multiplexing transmission using this Butler matrix and quickly reported a demonstration of 1.44 Tbps wireless transmission [31]. In this paper, we further improve our Butler matrix to increase the data rate and present the details of its design and performance that have not been presented. A summary of the contributions in this paper is as follows:

- *Versatile design methodology for wideband differential phase shifters (DPSs) used in our Butler matrix:* We focus on the dispersion curves of two waveguides and theoretically derive their geometries that give both the desired differential phase and gradient alignment of the dispersion curves enabling the uniform differential phase characteristics over a wide bandwidth. Since the DPSs include geometry variations in the width, we also propose a geometry design methodology for continuously tapered waveguides to facilitate micromachining. This methodology was derived on the basis of the characteristic impedance of the transmission medium, and the frequency is a tunable parameter, so it can be applied to both waveguides and transmission lines for any frequency band. The feasibility of this methodology was experimentally confirmed using waveguides.
- *Design and implementation of wideband high-precision sub-THz 8×8 Butler matrix for OAM multiplexing:* OAM multiplexing requires very high precision of DFT processing, and slight phase and amplitude errors cause intermodal interference. We designed a hollow-waveguide-based multi-layer 8×8 Butler matrix without crossover. This Butler matrix incorporates the aforementioned DPSs, geometry-optimized 3-dB couplers, and feeding networks to the UCA with an isoelectric lengths design. The fabricated 8×8 Butler matrix shows remarkable performance with low insertion loss of less than 1.5 dB and high mode isolation greater than 15 dB from 135 to 170 GHz for all OAM modes, and the average of the mode isolation within the band ranged from 19.2 to 25.2 dB.
- *Experimental demonstration of 1.58 Tbps physical-layer data rate with OAM multiplexing in the sub-THz bands:* A physical-layer data rate of 1.58 Tbps was recorded, experimentally outperforming current radio communications and the highest ever to the best of our knowledge. Note that the spatial multiplexing processing was performed only using the Butler matrix over the 32 GHz bandwidth in the sub-THz band, which would enable seamless connection to the other networks or utilization of generally commercialized high-speed digital signal processors for optical fiber communications in parallel without modification

The outline of this paper is as follows. In Section II, we provide an overview of the OAM multiplexing transmission technology. In Section III, we presents the multi-layer layout design of a hollow waveguide based Butler matrix, followed by the novel geometry design methodologies of its components, i.e., DPSs and 3-dB couplers. In Section IV, we present a three-dimensional (3D) model based on the layout design and performance evaluation of our prototype Butler matrix. Finally, in Section V, we discuss our OAM multiplexing transmission experiments using our Butler matrix in the sub-THz band and demonstration of a physical-layer data rate of 1.58 Tbps.

II. Overview of UCA-Based OAM Multipexing Transmission Technology

OAM beams are characterized by helical wavefronts, as shown in Fig. 1 (a). Fig. 1 (b) shows the phase distribution on a plane vertical to the beam propagation axis. The phase rotates linearly around the beam propagation axis at an integer multiple of 2π, guaranteeing a periodicity for circumferential direction that maintains the OAM states during propagation. Accordingly, the numbers representing the OAM modes take integer values, and their absolute values and signs represent the number of phase rotations and their directions, respectively.

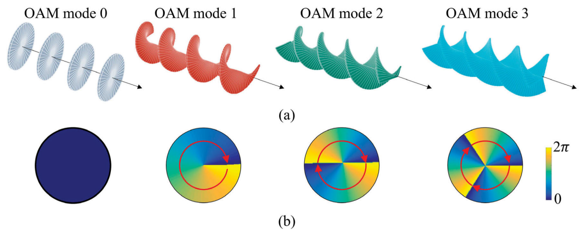

Fig. 1. (a) Wavefront of the OAM modes and (b) spatial phase distribution on a plane vertical to the propagation axis.

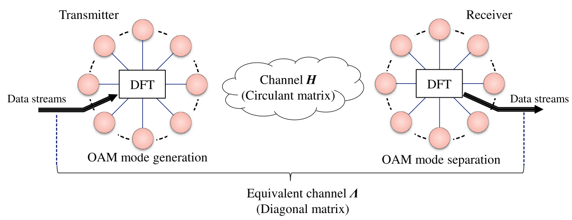

Fig. 2. Schematic of UCA based OAM multiplexing.

OAM mode 0 means the beam has no OAM, which is equivalent to a plane wave beam but is properly orthogonal to other beams with OAM. Note that the power distribution is uniform on the same circumference. Therefore, the OAM modes are circumferential Fourier modes.

Among the various methods of OAM multiplexing transmission, the mathematical background of that using oppositely arranged UCAs is described as follows. Fig. 2 shows a schematic of UCA-based OAM multiplexing. Let N be the number of antenna elements in a UCA, thus the channel-response matrix between oppositely arranged UCAs $\boldsymbol{H}_{\mathrm{OAM}} \in \mathbb{C}^{N\times N}$ is a circulant matrix because of the axisymmetric arrangement of the antenna elements. It is well known that the eigenvectors $\boldsymbol{d}_l$ of a circulant matrix are the Fourier modes and can be written explicitly as

$$\boldsymbol{d}_l = \left(1,\ v^l, v^{2l}, \cdots, v^{(N-1)l}\right)/\sqrt{N}, \tag{1}$$

where $v = \exp\left(2\pi j/N\right)$ is the complex N-th root unity and j is the imaginary unit. The OAM mode l takes an integer value from $\lceil -N/2 \rceil$ to $\lceil N/2 \rceil - 1$, where $\lceil * \rceil$ denotes the ceiling function. The phase gradient of $\frac{2l\pi}{K}$ given by v^l in $\boldsymbol{d}_l$ corresponds exactly to the phase distribution of the OAM mode l on the UCA. Note that the general range of l is denoted as 0 to $N-1$, but $\boldsymbol{d}_l$ and $\boldsymbol{d}_{l-N}$ is mathematically equivalent by definition, so it is defined in the aforementioned range to correspond to the number of phase rotations and the rotation direction of the OAM modes.

From these properties, the eigenvectors are the columns of the DFT matrix $D \in \mathbb{C}^{N\times N}$;

$$\boldsymbol{D} = \left[\boldsymbol{d}_{\lceil -N/2 \rceil} \quad \cdots \quad \boldsymbol{d}_l \quad \cdots \quad \boldsymbol{d}_{\lceil N/2 \rceil - 1}\right], \tag{2}$$

and $\boldsymbol{H}_{\mathrm{OAM}}$ is diagonalized by $\boldsymbol{D}$ as

$$\boldsymbol{\Lambda} = \boldsymbol{D}^H \boldsymbol{H}_{\mathrm{OAM}} \boldsymbol{D}, \tag{3}$$

$$\boldsymbol{\Lambda}_{p,q} = \begin{cases} \lambda_l & (p = q = l) \\ 0 & (p \neq q) \end{cases}, \tag{4}$$

where $*^H$ represents the Hermitian conjugate of a matrix, λ_l is the eigenvalue of $\boldsymbol{H}_{\mathrm{OAM}}$ corresponding to the channel coefficient of the OAM mode l, and $\boldsymbol{\Lambda}_{p,q}$ represents the element of the row and column corresponding to the eigenvectors $\boldsymbol{d}_p$ and $\boldsymbol{d}_q$, respectively. Thus, the OAM can be generated and separated by Fourier modes in the same way within its degrees of freedom even when spatially discretized by the array antenna.

Since the cyclicity of $\boldsymbol{H}_{\mathrm{OAM}}$ does not depend on the distance between UCAs, the multiplexing transmission process in the OAM modes is fixed as DFT processing, independent of the distance. In other words, the orthogonality between the OAM modes does not depend on the propagation distance, making deployment flexible, which is a strength of OAM multiplexing transmission. Moreover, the process corresponds to singular value decomposition, thus provides an upper bound on the capacity between UCAs derived from the MIMO theory as

$$C = \sum_l \left(1 + \frac{P_t \lambda_l}{\sigma^2}\right), \tag{5}$$

where σ^2 represents the power of white Gaussian noise and P_t is the transmitting power.

Then, OAM modes with higher $|l|$ have wider beam divergence resulting in lower eigenvalues, quantitatively [32]. Thus, when the variation in eigenvalues is very large, the number of utilized OAM modes can be limited to reduce, for example, hardware size and power consumption, since the modes with small eigenvalues contribute little to the capacity in (5). This trend occurs at distances farther than the Rayleigh distance, which is given by $d^2/2\lambda$ as a reference of transmission distance, where d is the diameter of UCAs and λ is the wavelength [19].

OAM and polarization can independently multiplex as degrees of freedom. A number of methods for enabling their combined use for multiplexing involve sharing each antenna element using a dual-polarized antenna or using double the number of UCAs and assigning half of them to one polarization [28]. Note that the axisymmetric distribution of the OAM restricts the propagation axis of only the multiplexed OAM beams, not necessarily the concentric arrangement of antennas for different polarization.

III. Layout and Components Design of Our 8×8 Butler Matrix

A. Layout Design of Our Butler Matrix

A Butler matrix is an analog beamforming circuit for multibeam antenna technologies [24]. A block diagram of an 8×8 Butler matrix circuit is shown in Fig. 3. The corresponding OAM modes are noted in parentheses next to the indexes of the input/output (I/O) ports. The Butler matrix is composed of 3-dB couplers and various DPSs, and it operates in a manner equivalent to that of the fast Fourier transform algorithm. However, the phase gradients given by the general $K \times K$ Butler matrix for beamforming with K antenna ports are $(2l+1)\,\pi/K$, which are partially different from the vectors of a DFT matrix in (1). Thus, the DPSs surrounded with a dotted frame in Fig. 3 are installed and the phase gradients are corrected to form integral-order OAM modes.

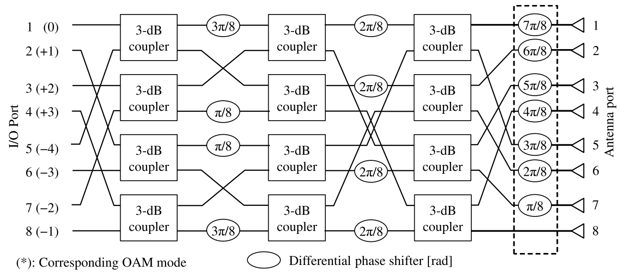

Fig. 3. Block diagram of an 8×8 Butler matrix for OAM multiplexing. The DPSs surrounded by a dotted frame are installed to obtain the orthogonal vectors of a DFT matrix.

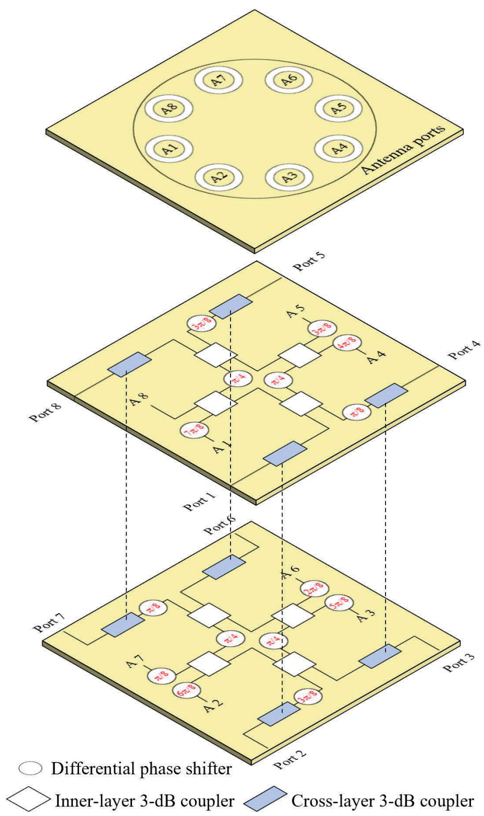

Fig. 4. Schematic design of our multi-layer 8×8 Butler matrix for OAM multiplexing.

Several techniques for constructing a Butler matrix have been reported, such as using microstrip lines [33], substrate integrated waveguides [35], and hollow waveguides [36]. In high-frequency bands, such as the sub-THz band, hollow waveguides have an advantage in terms of low insertion loss. Although the crossovers are often used where circuits intersect, they have a frequency dependence that leads to performance degradation, especially in wideband transmission. Since poor orthogonality due to circuit imperfections causes intermodal interference in OAM multiplexing transmission, a sufficiently high accuracy is required for this circuit over a wide bandwidth. Previous studies showed radiation patterns of the OAM beams using a Butler matrix or similar circuit [38], [39], [40]. However, in addition to being able to form OAM beams with spatial phase rotation, the crosstalk between OAM beams must be reduced and sufficient signal quality must be obtained to achieve OAM multiplexing transmission.

We design a rectangular hollow waveguide based multi-layer Butler matrix without crossover, as shown in Fig. 4. It has DPSs and two types of 3-dB couplers, cross-layer and inner-layer. Each cross-layer coupler connected with a dashed line is one across two layers. The waveguide can be manufactured by forming grooves in each of the several metal plates and fitting them together. Considering the transmission characteristics of a rectangular waveguide, the H-plane height does not affect to the propagation of fundamental mode TE10, but the E-plane width does. Therefore, we designed the waveguide orientation so that the E-plane of the rectangular waveguide is parallel to the split planes, i.e., the surface of each layer. In this way, the E-plane width can be precisely micro-machined on each metal plate, which prevents phase errors. Accordingly, the cross-layer and inner-layer couplers are E-plane and H-plane couplers, respectively. The waveguide ends labeled Ay ($y = 1, 2, \ldots, 8$) are connected to the corresponding antenna ports on the top layer through the feeding networks.

B. Design of Butler Matrix Components

The wavelength of the sub-THz waves is a few millimeters or less, so machining accuracy becomes a dominant hurdle to fabricate small and complex waveguides. The internal corners in the waveguide may have a slight but non-negligible roundness that causes unexpected performance errors. Thus, we investigated continuous geometries to avoid such errors and facilitate micromachining with end mills and similar tools. In this section, we propose geometry design methodologies for tapered waveguides and DPSs in which the waveguide width is continuously varied with low reflection. We then present the details of the geometry optimization design methodology of the 3-dB couplers based on a multi-objective optimization algorithm. Note that the effectiveness of these methodologies was confirmed experimentally.

1) Tapered Waveguide: In our waveguides, the geometries vary where the different components are connected and in the DPSs described in the following, so we first discuss the tapered waveguide and present a continuously-tapered-waveguide-design methodology that minimizes the reflection. To facilitate theoretical analysis, we then consider the fundamental mode TE10 and either keep the waveguide size under the cutoff frequency of higher modes or make its geometry symmetric to prevent the excitation of asymmetrical modes such as TE20 mode.

The characteristic impedance Z_0 in a rectangular waveguide with a E-plane width of a at an angular frequency ω is defined by

$$Z_0 = \frac{\omega \mu_0}{\sqrt{\varepsilon_r \left(\omega / c\right)^2 - \left(\pi / a\right)^2}}, \tag{6}$$

where c is the light speed, μ_0 is the magnetic permeability of free space, and ε_r is the relative permittivity. The reflection wave V_r shown in Fig. 5 is then derived by integrating the reflection waves at the tapered area of length L_t as follows, with the characteristic impedance at x as $Z_0(x)$:

$$V_r = \int_0^{L_t} \frac{1}{2Z_0(l)} \left(\frac{\partial Z_0(l)}{\partial l}\right) \exp\left(-2j\omega\mu_0 \int_0^{x} \left(\frac{du}{Z_0(l)}\right)\right) dl. \tag{7}$$

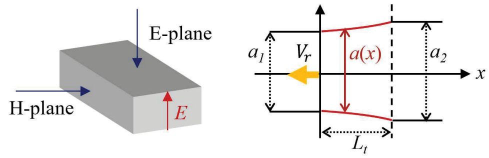

Fig. 5. E-plane view of the waveguide tapered section.

Let Z_{g1} and Z_{g2} be the characteristic impedance of waveguides of widths a_1 and a_2 at ω_c, respectively, which means that Z_{g1} and Z_{g2} are the characteristic impedances at $x = 0$ and L_t in Fig. 5. That is

$$Z_{g1} = \frac{\omega_c \mu_0}{\sqrt{\varepsilon_r \left(\frac{\omega_c}{c}\right)^2 - \left(\frac{\pi}{a_1}\right)^2}}, \tag{8}$$

$$Z_{g2} = \frac{\omega_c \mu_0}{\sqrt{\varepsilon_r \left(\frac{\omega_c}{c}\right)^2 - \left(\frac{\pi}{a_2}\right)^2}}. \tag{9}$$

To reduce the reflection, i.e., to solve $V_r = 0$, the characteristic impedance Z_c at ω_c is assumed to be a linear function of x as

$$Z_c(x) = \frac{(Z_{g2} - Z_{g1})}{L_t} x + Z_{g1}. \tag{10}$$

With this assumption, $Z_c(x)$ varies from Z_{g1} to Z_{g2} linearly and the waveguide geometry $a(x)$ shown in Fig. 5 is given by

$$a(x) = \pi \left(\varepsilon_r \left(\frac{\omega_c}{c}\right)^2 - \left(\frac{\omega_c \mu_0}{Z_c(x)}\right)^2 \right)^{-1/2}. \quad (0 \leq x \leq L_t) \tag{11}$$

Then, the length of the tapered section is derived as

$$L_t = \frac{m\pi}{\omega_c \mu_0} \frac{Z_{g1} - Z_{g2}}{\log(Z_{g1}/Z_{g2})}, \tag{12}$$

where m is a natural number, and $m = 1$ is used for all fabricated waveguides with the tapered section in this paper.

2) Differential Phase Shifter (DPS): Analog beamformers often require a constant phase difference between antennas in large relative bandwidth, which is especially important for OAM multiplexing. However, most DPSs adjust the phase shift by varying the length or width of the waveguides, but they are tuned to a specific frequency. To operate the DPS over a wide bandwidth, a number of DPSs such as corrugated structures [41] and glide-symmetric pin structures [42] have been proposed; however, the structures are rather complex, costly, and difficult to manufacture. Since the differential phase is basically not uniform over a wide bandwidth due to the wavelength-dispersion characteristics in waveguides, this section provides a theoretical design methodology for DPSs with simple and continuous geometries operating over a wide bandwidth.

Fig. 6 shows the design principle of our broadband DPSs derived from the dispersion curves of two waveguides. It is well known that the dispersion curves representing phase-frequency characteristics in waveguides are nonlinear curves unlike in free space. If the dispersion curves have not only a desired phase difference φ_s but also the same gradient at ω_c, the phase difference between the two waveguides may become uniform over a wide band.

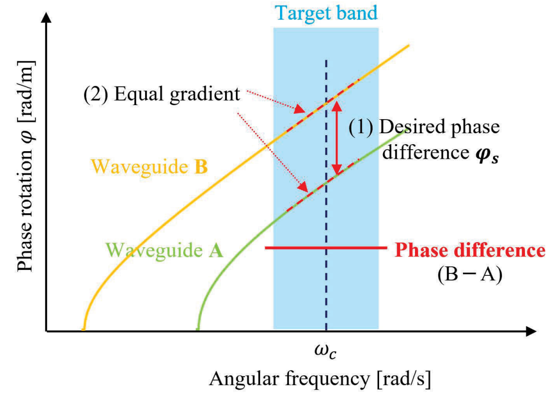

Fig. 6. Schematic of dispersion curves and phase difference between two waveguides with different.

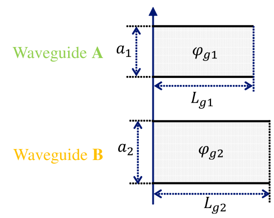

Fig. 7. E-plane view of two rectangular waveguides.

Therefore, we first simply assume two waveguides of different lengths and widths, as shown in Fig. 7, and set the objective functions as follows, with the phase rotation in waveguides A and B as φ_{g1} and φ_{g2}, respectively:

$$\varphi_{g1}(\omega_c) = \varphi_{g2}(\omega_c) + \varphi_s, \tag{13}$$

$$\frac{\partial \varphi_{g1}}{\partial \omega}(\omega_c) = \frac{\partial \varphi_{g2}}{\partial \omega}(\omega_c). \tag{14}$$

The phase rotation φ_g in a waveguide with a length of L is then given by

$$\varphi_g(\omega) = -\omega \mu_0 \int_0^L \frac{1}{Z_0(x)} dx. \tag{15}$$

Thus, the functions contained in (13) and (14) are derived from (15) as

$$\varphi_{g1}(\omega_c) = -\frac{\omega_c \mu_0 L_{g1}}{Z_{g1}}, \tag{16}$$

$$\varphi_{g2}(\omega_c) = -\frac{\omega_c \mu_0 L_{g2}}{Z_{g2}}, \tag{17}$$

$$\frac{\partial \varphi_{g1}}{\partial \omega}(\omega_c) = -L_{g1} \varepsilon_r \varepsilon_0 Z_{g1}, \tag{18}$$

$$\frac{\partial \varphi_{g2}}{\partial \omega}(\omega_c) = -L_{g2} \varepsilon_r \varepsilon_0 Z_{g2}. \tag{19}$$

From the aforementioned process, we obtain the geometries of the two waveguides by solving (13) and (14) simultaneously as

$$L_{g1} = \frac{\varphi_s Z_{g1} {Z_{g2}}^2}{\omega_c \mu_0 \left({Z_{g1}}^2 - {Z_{g2}}^2\right)}, \tag{20}$$

$$L_{g2} = \frac{\varphi_s {Z_{g1}}^2 Z_{g2}}{\omega_c \mu_0 \left({Z_{g1}}^2 - {Z_{g2}}^2\right)}. \tag{21}$$

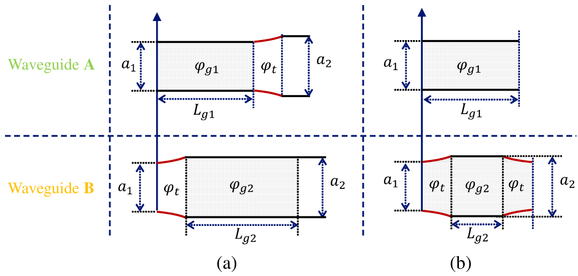

Fig. 8. Assumed DPSs geometries in waveguides.

When considering the implementation in a waveguide circuit, there are cases in which the phase shift is given while the widths of the two waveguides change from a_1 to a_2 (as shown in Fig. 8 (a)), and those of the two waveguides remain at a_1 (as shown in Fig. 8 (b)). Accordingly, the $\pi/4$ DPSs in Fig. 4 between the inter-layer 3-dB couplers have the geometry in Fig. 8 (b) and the other DPSs have the geometry in Fig. 8 (a). For the geometry in Fig. 8 (a), (20), and (21) can be applied directly, since the only difference between waveguides A and B is the gray regions, and the substantive condition is the same as that for Fig. 7. For the geometry in Fig. 8 (b), an additional phase rotation at the tapered section φ_t must be taken into account in waveguide B. Thus, the objective functions (13) and (14) become

$$\varphi_{g1}(\omega_c) = \varphi_{g2}(\omega_c) + 2\varphi_t(\omega_c) + \varphi_s, \tag{22}$$

$$\frac{\partial \varphi_{g1}}{\partial \omega}(\omega_c) = \frac{\partial \varphi_{g2}}{\partial \omega}(\omega_c) + 2\frac{\partial \varphi_t}{\partial \omega}(\omega_c), \tag{23}$$

where

$$\varphi_t(\omega_c) = -m\pi, \tag{24}$$

$$\frac{\partial \varphi_t}{\partial \omega}(\omega_c) = -\frac{m\pi}{2}\frac{\varepsilon_r\varepsilon_0}{\omega_c\mu_0}\frac{{Z_{g1}}^2 - {Z_{g2}}^2}{\log(Z_{g1}/Z_{g1})}. \tag{25}$$

Consequently, we obtain the geometries of the two waveguides by solving (22) and (23) simultaneously as

$$L_{g1} = \frac{Z_{g1}}{\omega_c\mu_0}\left\{\frac{m\pi}{\log(Z_{g1}/Z_{g2})} + \frac{{Z_{g2}}^2(\varphi_s - 2m\pi)}{{Z_{g1}}^2 - {Z_{g2}}^2}\right\}, \tag{26}$$

$$L_{g2} = \frac{Z_{g2}}{\omega_c\mu_0}\left\{\frac{m\pi}{\log(Z_{g1}/Z_{g2})} + \frac{{Z_{g1}}^2(\varphi_s - 2m\pi)}{{Z_{g1}}^2 - {Z_{g2}}^2}\right\}. \tag{27}$$

We then designed and fabricated 45°, 90°, 135°, and 180° DPSs to evaluate the performance of both the DPS and tapered waveguide design methodologies. Since the size of the I/O ports is based on the WR-06 standard flange specifications, the structure shown in Fig. 8 (b) was applied to the design with a_1 =1.651 mm. Fig. 9 shows the measured differential phase-frequency responses of the DPSs that have almost flat differential phase-frequency characteristics within the range of 135 to 170 GHz. Although a large differential phase results in a larger error at the edges of the band, the in-band standard deviation of phase error is 1.36° even for the 180° DPS. Note that the maximum differential phase in the layout of the Butler matrix is 157.5°. Fig. 10 shows the measured reflection frequency responses of the DPSs. Despite the included tapered sections, the reflection power was less than −30 dB.

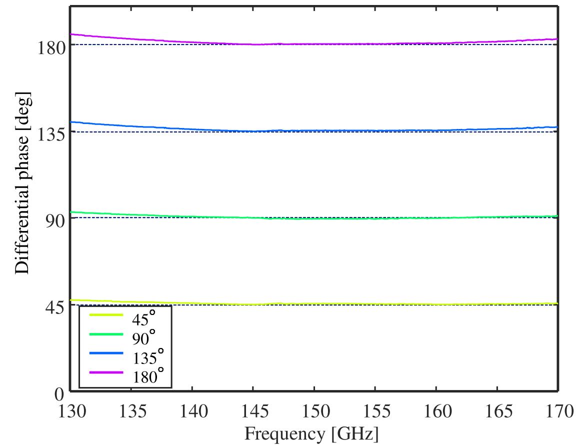

Fig. 9. Measured phase differences of 45°, 90°, 135°, and 180° DPSs.

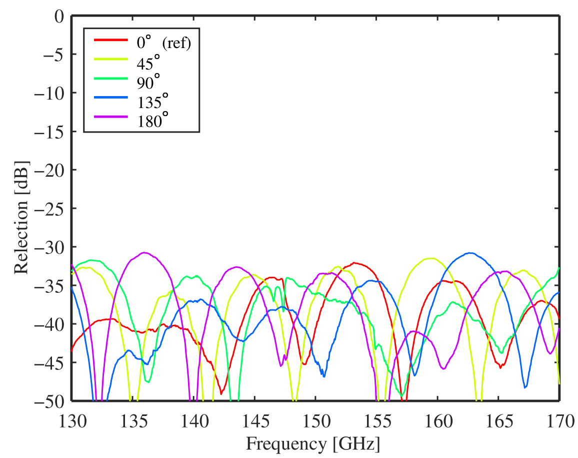

Fig. 10. Measured reflection properties of the DPSs with tapered sections.

3) Design of 3-dB Couplers: We designed two types of 3-dB couplers that are required in the layout of our Butler matrix: E-plane and H-plane couplers for the sub-THz band. We studied design methodologies to obtain a wideband performance with as simple geometries as possible and designed the E-plane and H-plane couplers on the basis of the multi-branch coupler [43], [44] and short slot coupler [45], [46], [47], respectively. However, in theoretical designs, the corners are right-angled, so it is necessary to give roundness to a number of corners for micromachining. Therefore, after rounding a number of corners, the geometries were optimized by parametric studies using a multi-objective optimization algorithm based on the Kriging response surface model using HFSS, which is full-wave 3D electromagnetic simulation software. Note that the required performance of the 3-dB couplers is that the transmit power (S31 and S41) should be equally −3 dB over a wide bandwidth and that the reflection loss (S11 and S21) be as low as possible.

Fig. 11 shows the geometries of the E-plane and H-plane couplers. A number of corners are rounded to a radius of 0.1 mm. Note that the H-plane coupler has a groove at the coupling section to give more degrees of freedom for optimization and to obtain better characteristics. The coupling section of the H-plane coupler is wider, enabling multiple transmission modes to exist. The current distribution on the E-plane in a wide waveguide is shown in Fig. 12. Note that the waveguide

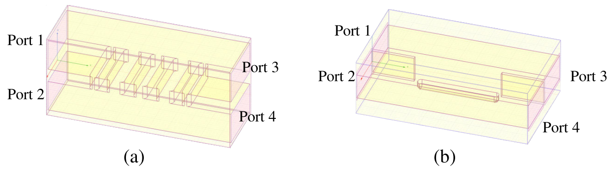

Fig. 11. Geometries of (a) E-plane coupler and (b) H-plane coupler.

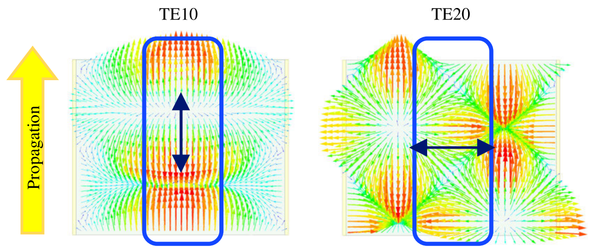

Fig. 12. Current distribution on the E-plane of a rectangular waveguide with a width greater than the wavelength where the TE10 and TE20 modes exist.

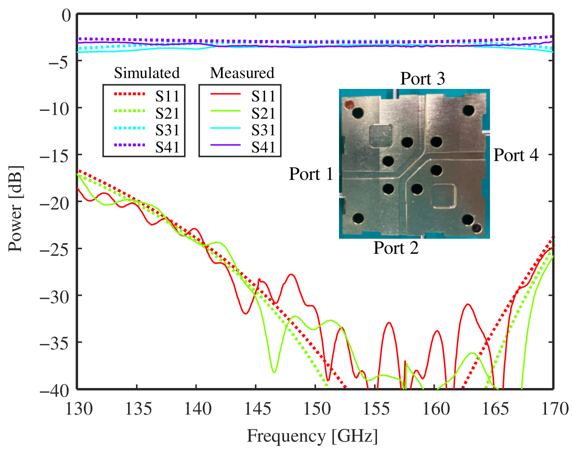

Fig. 13. Simulated and Measured S-parameters of the H-plane coupler with a groove at the coupling section.

operates as a 3-dB coupler when the phase rotation in the coupling section is exactly a 90° difference between the TE10 and TE20 modes. The TE10 mode has currents only parallel to the propagation direction in the center of the coupling section (surrounded with a blue frame), whereas the TE20 mode has currents transverse to the propagation direction. Accordingly, the propagation of the TE20 mode was controlled by forming a ridge or groove on the E-plane parallel to the propagation direction. For the H-plane coupler, a prototype was fabricated to verify the effect of the newly formed groove structure. Fig. 13 shows the simulated and measured S-parameters of the H-plane coupler. The measurement results showed agree with the simulated results, and the measured amplitude imbalance of S31 and S41 was 0.29 dB and the reflections were smaller than −20 dB from 135 to 170 GHz.

C. 3D Model Design of Butler Matrix

On the basis of the above discussion and layout design, we designed a 3D model of our Butler matrix. Fig. 14 shows the 3D model and fabricated prototype of our Butler matrix. The 3D model includes feeding networks to the antenna ports that are arranged in a circle uniformly as the UCA. Note that the feeding networks are wired so that the angle and number of bends are aligned, and the electrical lengths are the same. The 3D model is divided into five metal plates, which are

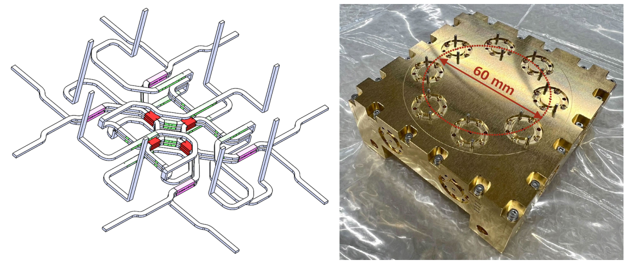

Fig. 14. One side view of the representative layer including all components designed in this paper.

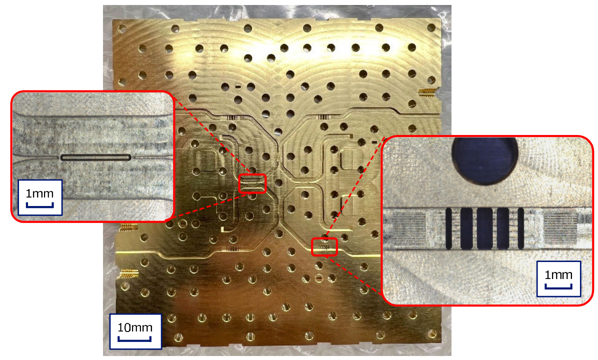

Fig. 15. One side view of the representative layer including all components designed in this paper.

precisely engaged and screwed together. The two layers in the layout, containing the 3-dB couplers and DPSs, are formed by grooving both sides of a single metal plate and covering it from both sides; one side of the metal plate is shown in Fig. 15.

IV. Performance Evaluation of Prototype Butler Matrix

Fig. 16 shows the measured differential phases of each antenna port relative to the phase of antenna port 1 (A1). They all are very uniform over the wide band, and the average phase imbalance of all OAM modes was 3.03° in the 135–170 GHz band. We then evaluated the mode isolation of our Butler matrix, which is defined as the ratio of the power of the desired OAM mode to that of the intermodal interference to or from the other OAM modes. Thus, the mode isolation index represents the OAM spectrum purity generated from the Butler matrix. If the Butler matrix was operating correctly as a DFT processor, the measured S-parameter $\boldsymbol{S}$ should revert to a diagonal matrix through the inverse-DFT (IDFT) process. Therefore, let $\boldsymbol{R}$ denote the IDFT-processed $\boldsymbol{S}$, which is expressed as

$$\boldsymbol{R} = \boldsymbol{D}^H \boldsymbol{S}, \tag{28}$$

where each diagonal component of $\boldsymbol{R}$ represents the gain of the corresponding OAM mode, and the other components represent that of the intermodal interference. Thus, the mode isolation γ_l for OAM mode l is defined as

$$\gamma_l = \frac{|\boldsymbol{R}_{l,l}|^2}{\sum_{x \neq l} |\boldsymbol{R}_{l,x}|^2}, \tag{29}$$

where $\boldsymbol{R}_{p,q}$ represents the element of the row and column corresponding to OAM modes p and q. Fig. 17 shows the

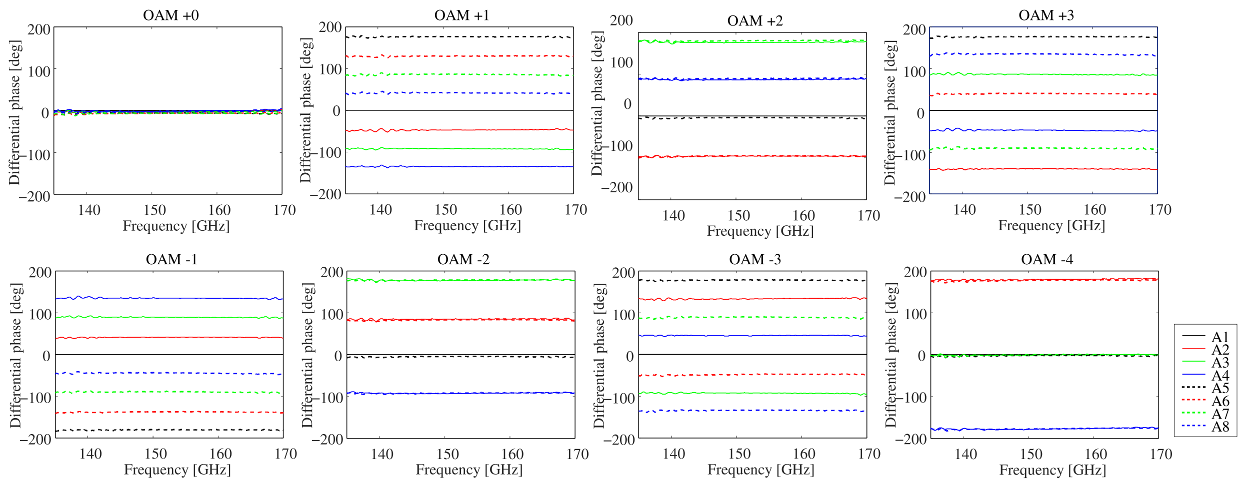

OAM mode	−4	−3	−2	−1	0	+1	+2	+3	All
Imbalance (degree)	1.97	2.05	3.75	1.63	4.19	2.95	3.70	2.95	3.03

Fig. 16. Measured differential phase between antenna ports (A1–8) relative to antenna port 1 (A1) and standard deviation of differential phase imbalance from 135 to 170 GHz.

TABLE I
COMPARISON BETWEEN THE REPORTED BUTLER MATRICES FOR BEAMFORMING

Ref.	[33]	[34]	[35]	[36]	[37]	This work
Technology	Microstrip line	Finline	SIW	WG	Gap WG	WG
Frequency [GHz]	1.98–3.14	74.0–82.5	28.0–32.0	19.3–19.7	77.5–92.5	135–170
Fractional bandwidth [%]	45.3	11	13.3	2.1	17.6	23
Order	4×4	4×4	4×4	64×64	4×4	8×8
Return loss [dB]	−10	−10	−10	−10	−10	−17.5
Insertion loss [dB]	0.8	2.42	1.8	1.8	1.17	1.46
Amplitude imbalance [dB]	1	–	1	4	1.5	0.41
Phase imbalance [degree]	7	16	11	40	17	3.03

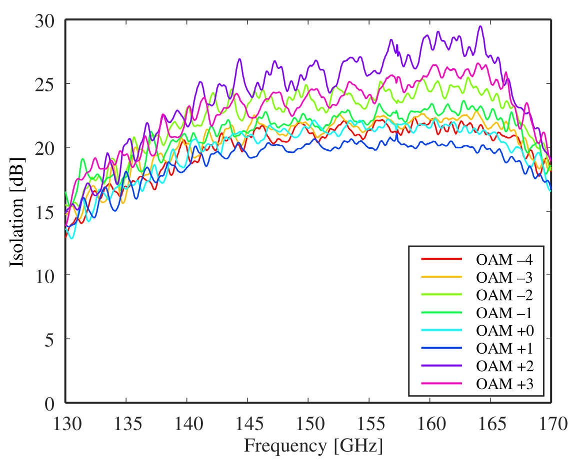

Fig. 17. Mode isolation of a fabricated Butler matrix for each OAM mode.

mode isolation for each OAM mode. The mode isolation was greater than 15 dB from 135 to 170 GHz for all OAM modes, and the average within the band ranged from 19.2 to 25.2 dB. Since the wavelength of the sub-THz band is very short (a few mm), the variation in isolation values for the OAM modes could be better controlled by improving manufacturing accuracy. Fig. 18 shows the frequency response of the gain for each OAM mode corresponding to $|\boldsymbol{R}_{l,l}|^2$ in (29), and reflection characteristics measured at I/O ports. Despite the large scale of the waveguide, the average losses for all OAM modes were less than 1.5 dB from 135 to 170 GHz. Note that the losses include not only the conductor resistive losses but also reflections and leakage into undesired OAM modes. The reflection was less than −20 dB in the same frequencies. Table I shows a performance comparison with previously reported Butler matrices for beamforming. Our Butler matrix achieves much higher operation frequency, lower return loss, and less amplitude/phase imbalance over a wide bandwidth.

V. EXPERIMENT ON OVER 1 TBPS WIRELESS TRANSMISSION

Fig. 19 shows the configuration of our OAM multiplexing transmission experimental system for the sub-THz band, and Table II lists the specific parameters of our experimental setup. An offline DSP is implemented in parallel for each OAM mode, and the Butler matrices perform the generation and separation of the spatially superposed OAM beams, so additional equalization processing between the OAM modes is not required. Digital intermediate frequency (IF, 0.5–16.5 GHz) waveforms are created with an adaptive quadrature amplitude modulation (QAM) system of a single carrier with frequency domain equalization (SC-FDE) [48].

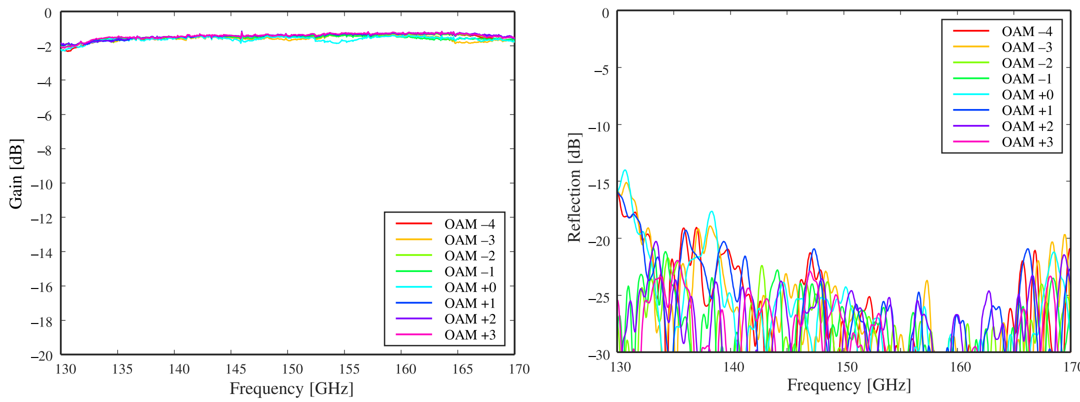

(a) Gain property

(b) Reflection characteristics

Fig. 18. (a) Gain property for each OAM mode and (b) reflection characteristics measured at I/O ports.

Data streams are coded with low density parity-check (LDPC) code and Bose-Chaudhuri-Hocquenghem (BCH) code on the basis of a standard for digital video broadcasting second generation (DVB-S.2) [49] used as forward error collection (FEC). The quasi error free (QEF) quality is defined in the DVB-S.2, which approximately corresponds to a packet error ratio PER $< 10^{-7}$. Since the DVB-S.2 standard modulation specification is phase shift keying (PSK), the performance requirements of the ratio between the energy per symbol to noise power (E_s/N_0) for QAM are calculated in the same manner through numerical simulation. Table III summarizes the performance requirements at the QEF over additive white Gaussian noise. In our offline DSP, the modulations and coding rates are adaptively determined, and the data rates are measured as the sum rates of the transmission satisfying the QEF quality in each of the eight OAM modes. Digital-to-analog and analog-to-digital conversion are executed using synchronized arbitrary waveform generators (AWGs, Keysight M8195A) and a digital sampling oscilloscope (Tektronix DPO72304X), respectively. Up- and down-conversion between IF and RF are executed using subharmonic mixers (VDI WR6.5CCU/CCD). The local signals are supplied from signal generators (R&S SMB100A) to the subharmonic mixers, which multiply the local signals by six for the up- and down-conversion. The power amplifiers (PAs, VDI WR6.5AMP, 20 dB gain) and low noise amplifiers (LNAs, Radiometer, 15 dB gain, 6 dB noise figure) are placed before and after the Butler matrices at the transmitter (Tx) and receiver (Rx), respectively, since they cause phase and amplitude imbalance. Note that the peak-to-average power ratio increases at the antennas due to the combination of multiple OAM modes and exceeds the waveguide losses in our configuration, which is another reason that the amplifiers are placed in the configuration. Since the receiving UCA is placed opposite the transmitting UCA, the coordinate system is inverted and the process in the receiving Butler matrix is equivalent to the IDFT. Therefore, the OAM mode and I/O port correspondence shown in Fig. 3 are the same for the transmitter and receiver.

Fig. 20 shows a photograph of our experimental system constructed in the shield room. The propagation axes of the oppositely arranged UCAs are aligned using optical lasers and fine-tuned to minimize the intermodal interferences. The alignment is required once before transmission and all OAM waves are transmitted simultaneously. The diameter of the UCAs is 6 cm, and the Rayleigh distance in this case is roughly 0.9 m, so all OAM modes are considered available at a distance of 1 m. This distance can be extended arbitrarily by enlarging the diameter of UCAs or using parabolic reflectors [50] or dielectric lens [51] to expand the effective diameter of the UCAs. From the definition of the Rayleigh distance ($d^2/2\lambda$) [19], the achievable transmission distance is proportional to the square of the diameter of a UCA. For a transmission distance

TABLE II

PARAMETERS OF OUR EXPERIMENTAL SETUP

Radio frequency	136–152 GHz / 152–168 GHz
Bandwidth	16 GHz × 2
Polarization	2 (horizontal and virtical)
Distance	1 m
Transmission power	5 dBm (−4 dBm/stream)
OAM mode	−4, −3, −2, −1, 0, 1, 2, 3
No. of antenna elements	8 elements / UCA
Diameter of UCA	6 cm
Error correction	LDPC & BCH (DVB-S.2)
Prepared LDPC coding rate	1/4, 1/3, 2/5, 1/2, 3/5, 2/3, 3/4, 4/5, 5/6, 8/9, 9/10
Equalization algorithm	SC-FDE
Frame length	32,400 symbols
Modulation	QPSK, 16QAM, 64QAM

TABLE III

E_S/N_0 PERFORMANCE AT QUASI ERROR FREE PER $= 10^{-7}$

Mode		E_s/N_0 [dB]	Mode		E_s/N_0 [dB]
QPSK	1/4	−2.35	16QAM	2/3	8.82
QPSK	1/3	−1.24	16QAM	3/4	10.08
QPSK	2/5	−0.30	16QAM	4/5	10.84
QPSK	1/2	1.00	16QAM	5/6	11.42
QPSK	3/5	2.23	64QAM	3/5	12.66
QPSK	2/3	3.10	64QAM	2/3	13.72
QPSK	3/4	4.03	64QAM	3/4	15.24
16QAM	2/5	4.61	64QAM	4/5	16.23
QPSK	5/6	5.28	64QAM	5/6	16.93
16QAM	1/2	6.30	64QAM	8/9	18.32
16QAM	3/5	7.88	64QAM	9/10	18.57

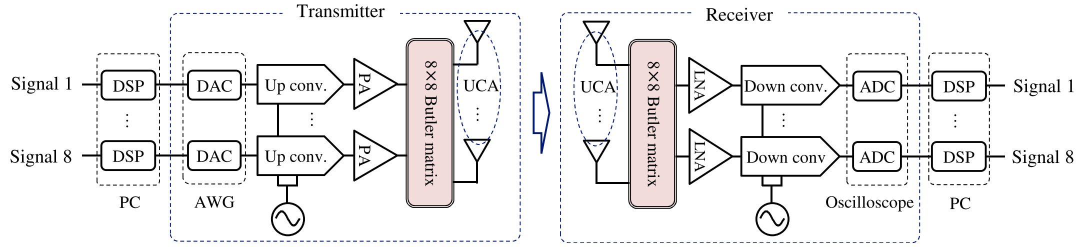

Fig. 19. Configuration of our OAM multiplexing transmission system.

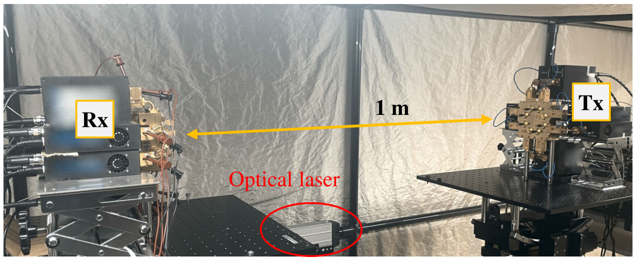

Fig. 20. Photograph of our experimental system in a shielded room. The transmitting and receiving UCAs were mechanically aligned using an optical laser.

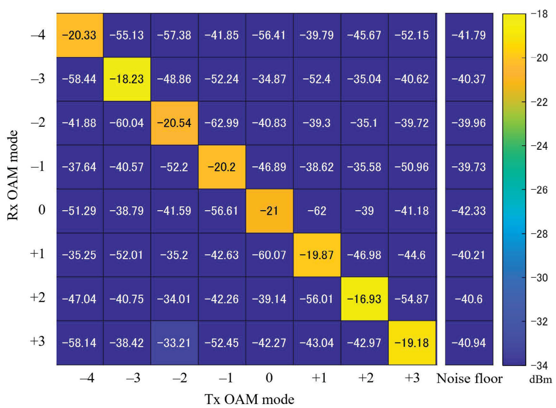

(a) 136-152 GHz

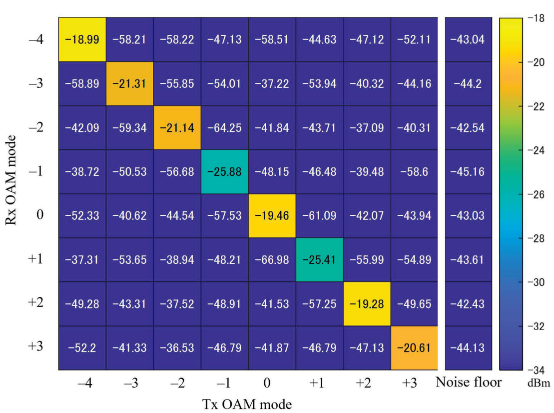

(b) 152-168 GHz

Fig. 21. Measured equivalent channel responses between transmitter and receiver in the 136–152 GHz and 152–168 GHz bands at a distance of 1 m.

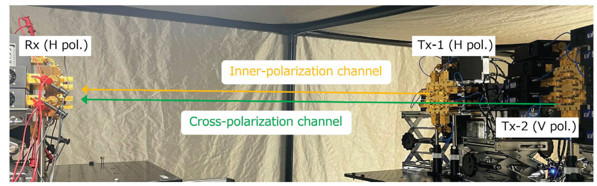

(a)

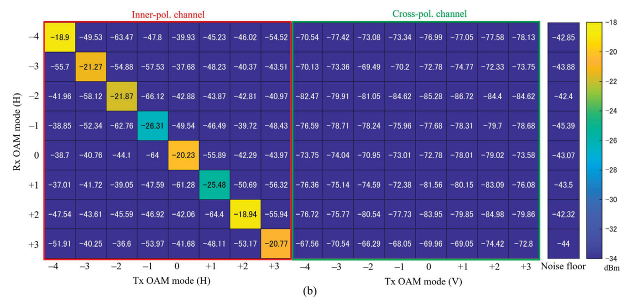

(b)

Fig. 22. (a) Photograph of cross-polarization experimental system and (b) measured inner- and cross-polarization channels in the 152–168 GHz band.

of 100 m, for example, an effective UCA diameter of 60 cm would give eigenvalues approximately equivalent to those for the configuration in this experiment.

Fig. 21 shows the channel-response matrices of the received signal power at a distance of 1 m. Each signal power was measured using a dedicated preamble with an orthogonal sequence. Ideally, the channel response should be a diagonal matrix, as in (4), and the non-diagonal components are intermodal interference. They include the effects of all receiving devices, such as circuit losses shown in Fig. 18, cable losses, amplifier gain, and quantization noise, so the noise level at the receiving end is also listed for reference. With such a wideband transmission, the quantization noise in the analog-to-digital converter (ADC) is one of the dominant factors, so the noise level varies with the received signal power. The OAM modes with the same $|l|$ are basically identical transmission characteristics because of the symmetrical spatial distribution, although there are slight differences due to variations in the gain characteristics of the RF amplifiers and the other RF devices. The channel response matrices represent our OAM multiplexing transmission system quality and show the effect of the transmitting and receiving Butler matrices and transmission paths on intermodal interference. Thus, the higher the mode isolation of the prototype Butler matrix shown in Fig. 17, and the lower the error factors such as misalignment and multipath, the lower the intermodal interference components and the closer the channel response matrix approaches the diagonal matrix.

Next, we investigated the impact of cross-polarization interference. Due to the convenience of the measurement, the receiving signal power between the vertical and horizontal polarization was measured by arranging two Tx antennas side-by-side with different polarization. Fig. 22 (a) shows a photograph of the experimental system. Transmission was executed between the Tx-1 and Rx with horizontal polarization

TABLE IV
EXPERIMENTAL RESULTS OF PHYSICAL LAYER DATA RATES

Frequency	136–152 GHz				152–168 GHz			
OAM mode	E_s/N_0 [dB]	Modulation (Coding rate)	Spectrum efficiency	Data rate [Gbit/s]	E_s/N_0 [dB]	Modulation (Coding rate)	Spectrum efficiency	Data rate [Gbit/s]
0	10.90	16 QAM (3/4)	2.9881	47.810	14.38	64 QAM (2/3)	3.9852	63.763
+1	10.16	16 QAM (2/3)	2.6568	42.509	6.67	16 QAM (1/2)	1.9881	31.810
+2	12.82	16 QAM (5/6)	3.3235	53.175	13.33	64 QAM (3/5)	3.5822	57.316
+3	10.30	16 QAM (2/3)	2.6568	42.509	11.48	16 QAM (4/5)	3.1881	51.010
−1	9.53	16 QAM (2/3)	2.6568	42.509	6.77	16 QAM (1/2)	1.9881	31.810
−2	9.55	16 QAM (2/3)	2.6568	42.509	10.62	16 QAM (3/4)	2.9881	47.810
−3	11.24	16 QAM (4/5)	3.1881	51.010	11.79	16 QAM (5/6)	3.3235	53.175
−4	13.23	64 QAM (3/5)	3.5822	57.316	17.10	64 QAM (4/5)	4.7822	76.516

Frequency	Data rate	Sum data rate (single pol.)	Sum data rate (dual pol.)
136–152 GHz	379.34 Gbit/s	792.55 Gbit/s	1.58 Tbit/s
152–168 GHz	413.21 Gbit/s		

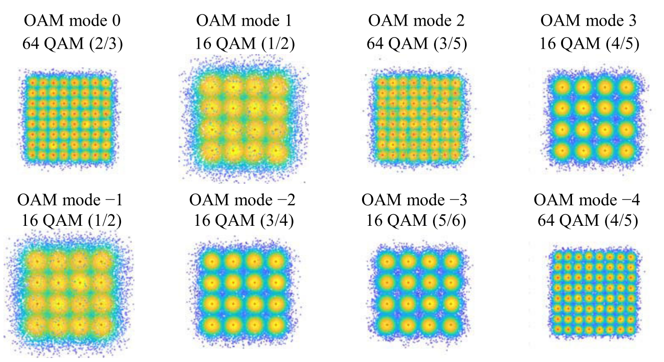

Fig. 23. Representative constellations of the transmitted signals in the 152–168 GHz band.

(H pol.), and the Tx-2 transmitted signals with vertical polarization (V pol.) at the same time, which resulted in cross-polarization interference. Since the signals were all transmitted simultaneously, this is equivalent to the cross-polarization interference conditions during dual-polarization parallel transmission. Fig. 22 (b) shows the measured inner- and cross-polarization channels in the 152–168 GHz band. The notation is the same as that in Fig. 21, and the elements within the same polarization and between different polarizations are framed in red and green, respectively. Since the noise floor was a minimum of -47.39 dBm and the receiving power of cross-polarization was less than -66.29 dBm, the cross-polarization interference was all less than -20 dB relative to the noise floor, which was negligible. There was no difference in transmission data rates with or without cross-polarization interference, and the OAM and polarization could be used independently and simultaneously, confirming that the data rate can be doubled using dual polarization.

Table IV summarizes the experimental results of the physical-layer data rates. The E_s/N_0, modulation, LDPC coding rate, and spectrum efficiency of each OAM mode and frequency band are also listed. Fig. 23 shows representative constellations of the transmitted signals on the OAM modes in the 152–168 GHz band. As mentioned earlier, the modulation and coding rate were adaptively determined in accordance with their signal quality in advance, and the transmission channel in the fixed LoS environment was stable, so all measured E_s/N_0 values were beyond the QEF quality shown in Table III. For reference, no bit error occurred after decoding in a few dozen of signal frames by which the constellations were obtained. We confirmed a total physical-layer data rate of 1.58 Tbps in the sub-THz band using eight OAM modes and dual polarization without digital equalization between them.

VI. Conclusion

We proposed a wideband hollow waveguide based Butler matrix for the sub-THz band and presented a demonstration of 1.58 Tbps wireless transmission on the basis of OAM multiplexing technology using our Butler matrix was presented. Our Butler matrix has a multi-layer layout and composed of DPSs and 3-dB couplers. The geometric design methodology for the DPSs and that for the 3-dB couplers were devised on the basis of the parametric optimization algorithm. Note that the aforementioned contributions of this paper facilitate fabricating a waveguide Butler matrix in different target bands. The prototype Butler matrix showed losses of less than 1.5 dB and a mode isolation of more than 15 dB from 135 to 170 GHz. We then constructed an OAM multiplexing transmission experimental system using the prototype Butler matrices in the sub-THz band and demonstrated 1.58 Tbps wireless transmission at a distance of 1 m using eight OAM modes and dual polarization, which is the highest data rate achieved in wireless radio transmission to the best of our knowledge. The transmission distance can be extended by using parabolic reflectors or dielectric lens to expand the effective antenna size on a Butler matrix, so we believe that the OAM multiplexing transmission system with our Butler matrix can provide terabit-class wireless backhaul and fronthaul for distances over 100 m by designing the appropriate effective antenna size. Note that DSP was independently processed in each data stream, where no equalization between the streams was applied since all multiplexing processing was conducted in the Butler matrices. Therefore, physical-layer processing, such as modulation and demodulation schemes, can be generic for single stream transmission and highly compatible with generally commercialized high-speed digital signal processors such as those for fiber optics communications to provide low-cost real-time communication systems.

References

[1] *3GPP*. Accessed: May 1, 2024. [Online]. Available: https://www.3gpp.org/

[2] NTT DOCOMO. (2020). *DOCOMO 6G White Paper*. [Online]. Available: https://www.nttdocomo.co.jp/english/info/media_center/pr/2020/0124_00.html

[3] SAMSUNG. *SAMSUNG 6G Vision*. Accessed: May 1, 2024. [Online]. Available: https://research.samsung.com/next-generation-communications

[4] Y. Corre. (Mar. 2019). *Sub-THz Spectrum As Enabler for 6G Wireless Communications Up To 1 Tbps*. [Online]. Available: http://www.6gsummit.com/wp-content/uploads/2019/04/Day3_Session7_Corre_SIRADEL.pdf

[5] B. Tezergil and E. Onur, "Wireless backhaul in 5G and beyond: Issues, challenges and opportunities," *IEEE Commun. Surveys Tuts.*, vol. 24, no. 4, pp. 2579–2632, 4th Quart., 2022.

[6] S. Ni, J. Zhao, H. H. Yang, and Y. Gong, "Enhancing downlink transmission in MIMO HetNet with wireless backhaul," *IEEE Trans. Veh. Technol.*, vol. 68, no. 7, pp. 6817–6832, Jul. 2019.

[7] Z. Zhang, X. Wang, K. Long, A. V. Vasilakos, and L. Hanzo, "Large-scale MIMO-based wireless backhaul in 5G networks," *IEEE Wireless Commun.*, vol. 22, no. 5, pp. 58–66, Oct. 2015.

[8] C. Castro, R. Elschner, T. Merkle, C. Schubert, and R. Freund, "Experimental demonstrations of high-capacity THz-wireless transmission systems for beyond 5G," *IEEE Commun. Mag.*, vol. 58, no. 11, pp. 41–47, Nov. 2020.

[9] X. Li et al., "1-Tb/s millimeter-wave signal wireless delivery at D-band," *J. Lightw. Technol.*, vol. 37, no. 1, pp. 196–204, Jan. 1, 2019.

[10] R. Igarashi et al., "First demonstration of 128-Gbit/s 300-GHz-band THz transmission using OFC-based transmitter and intradyne receiver," in *Proc. 27th OECC PSC*, Toyama, Japan, 2022, pp. 1–3.

[11] C. Huang et al., "Holographic MIMO surfaces for 6G wireless networks: Opportunities, challenges, and trends," *IEEE Wireless Commun.*, vol. 27, no. 5, pp. 118–125, Oct. 2020.

[12] E. Björnson and L. Sanguinetti, "Power scaling laws and near-field behaviors of massive MIMO and intelligent reflecting surfaces," *IEEE Open J. Commun. Soc.*, vol. 1, pp. 1306–1324, 2020.

[13] J. Zhao et al., "Programmable time-domain digital-coding metasurface for non-linear harmonic manipulation and new wireless communication systems," *Nat. Sci. Rev.*, vol. 6, no. 2, pp. 231–238, Mar. 2019.

[14] L. Zhang et al., "A wireless communication scheme based on space- and frequency-division multiplexing using digital metasurfaces," *Nature Electron.*, vol. 4, no. 3, pp. 218–227, Mar. 2021.

[15] Y. Yan et al., "High-capacity millimeter-wave communications with orbital angular momentum multiplexing," *Nature Commun.*, vol. 5, p. 4876, Sep. 2014.

[16] L. Cheng, W. Hong, and Z.-C. Hao, "Generation of electromagnetic waves with arbitrary orbital angular momentum modes," *Sci. Rep.*, vol. 4, no. 1, pp. 4814–4818, Apr. 2014.

[17] F. E. Mahmouli and S. D. Walker, "4-Gbps uncompressed video transmission over a 60-GHz orbital angular momentum wireless channel," *IEEE Wireless Commun. Lett.*, vol. 2, no. 2, pp. 223–226, Apr. 2013.

[18] X. Qi, Z. Zhang, X. Zong, X. Que, Z. Nie, and J. Hu, "Generating dual-mode dual-polarization OAM based on transmissive metasurface," *Sci. Rep.*, vol. 9, no. 1, p. 97, Jan. 2019.

[19] O. Edfors and A. J. Johansson, "Is orbital angular momentum (OAM) based radio communication an unexploited area?" *IEEE Trans. Antennas Propag.*, vol. 60, no. 2, pp. 1126–1131, Feb. 2012.

[20] S. M. Mohammadi et al., "Orbital angular momentum in radio—A system study," *IEEE Trans. Antennas Propag.*, vol. 58, no. 2, pp. 565–572, Feb. 2010.

[21] R. M. Henderson, "Let's do the twist!: Radiators, experiments, and techniques to generate twisted waves at radio frequencies," *IEEE Microw. Mag.*, vol. 18, no. 4, pp. 88–96, Jun. 2017.

[22] J. Wang et al., "Terabit free-space data transmission employing orbital angular momentum multiplexing," *Nature Photon.*, vol. 6, no. 7, pp. 488–496, Jul. 2012.

[23] N. Bozinovic et al., "Terabit-scale orbital angular momentum mode division multiplexing in fibers," *Science*, vol. 340, no. 6140, pp. 1545–1548, Jun. 2013.

[24] A. B. Shallah et al., "Recent developments of Butler matrix from components design evolution to system integration for 5G beamforming applications: A survey," *IEEE Access*, vol. 10, pp. 88434–88456, 2022.

[25] F. Sohrabi and W. Yu, "Hybrid digital and analog beamforming design for large-scale antenna arrays," *IEEE J. Sel. Topics Signal Process.*, vol. 10, no. 3, pp. 501–513, Apr. 2016.

[26] B. Liu, Y. Cui, and R. Li, "A broadband dual-polarized dual-OAM-mode antenna array for OAM communication," *IEEE Antennas Wireless Propag. Lett.*, vol. 16, pp. 744–747, 2017.

[27] H. Sasaki et al., "Experiment on over-100-Gbps wireless transmission with OAM-MIMO multiplexing system in 28-GHz band," in *Proc. IEEE Global Commun. Conf. (GLOBECOM)*, Abu Dhabi, UAE, Dec. 2018, pp. 1–6.

[28] Y. Yagi, H. Sasaki, T. Yamada, and D. Lee, "200 Gbit/s wireless transmission using dual-polarized OAM-MIMO multiplexing on 28 GHz band," in *Proc. IEEE Globecom Workshops (GC Wkshps)*, Waikoloa, HI, USA, Dec. 2019, pp. 1–4.

[29] H. Sasaki, Y. Yagi, T. Yamada, and D. Lee, "Field experimental demonstration on OAM-MIMO wireless transmission on 28 GHz band," in *Proc. IEEE Globecom Workshops (GC Wkshps)*, Waikoloa, HI, USA, Dec. 2019, pp. 1–4.

[30] D. Lee, H. Sasaki, Y. Yagi, and H. Shiba, "Orbital angular momentum multiplexing using radio wave and its extension to multishape radio," *J. Lightw. Technol.*, vol. 41, no. 7, pp. 1985–1996, Apr. 1, 2023.

[31] H. Sasaki, Y. Yagi, R. Kudo, and D. Lee, "Demonstration of 1.44 Tbit/s OAM multiplexing transmission in sub-THz bands," in *Proc. IEEE Int. Conf. Commun. Workshops (ICC Workshops)*, Roma, Italy, May 2023.

[32] M. J. Padgett, F. M. Miatto, M. P. J. Lavery, A. Zeilinger, and R. W. Boyd, "Divergence of an orbital-angular-momentum-carrying beam upon propagation," *New J. Phys.*, vol. 17, no. 2, Feb. 2015, Art. no. 023011.

[33] J. M. Wen, C. K. Wang, W. Hong, Y. M. Pan, and S. Y. Zheng, "A wideband switched-beam antenna array fed by compact single-layer Butler matrix," *IEEE Trans. Antennas Propag.*, vol. 69, no. 8, pp. 5130–5135, Aug. 2021.

[34] N. T. Tuan, K. Sakakibara, K. Iwasa, T. Okunaga, N. Kikuma, and Y. Sugimoto, "Millimeter-wave Butler matrix beamforming circuit using finline in double-layer dielectric substrate," *IEEE Open J. Antennas Propag.*, vol. 1, pp. 579–589, 2020.

[35] Q. Sun, Y.-L. Ban, Y.-X. Che, and Z. Nie, "Coexistence-mode CRLH SIW transmission line and its application for longitudinal miniaturized Butler matrix and multibeam array antenna," *IEEE Trans. Antennas Propag.*, vol. 69, no. 11, pp. 7593–7603, Nov. 2021.

[36] T. Tomura, D.-H. Kim, M. Wakasa, Y. Sunaguchi, J. Hirokawa, and K. Nishimori, "A 20-GHz-band 64×64 hollow waveguide two-dimensional Butler matrix," *IEEE Access*, vol. 7, pp. 164080–164088, 2019.

[37] C. Wang, Y. Yao, X. Cheng, Z. Zhu, and X. Li, "A W-band high-efficiency multibeam circularly polarized antenna array fed by GGW Butler matrix," *IEEE Antennas Wireless Propag. Lett.*, vol. 20, no. 7, pp. 1130–1134, Jul. 2021.

[38] W. Lee et al., "Microwave orbital angular momentum mode generation and multiplexing using a waveguide Butler matrix," *ETRI J.*, vol. 39, no. 3, pp. 336–344, Jun. 2017.

[39] W. J. Byun et al., "Multiplexed Cassegrain reflector antenna for simultaneous generation of three orbital angular momentum (OAM) modes," *Sci. Rep.*, vol. 6, no. 1, Jun. 2016, Art. no. 27339.

[40] N.-W. Chen, R.-R. Guo, and J.-W. Shi, "Millimeter-wave orbital angular momentum radiations from photonic-based transmitter," in *Proc. IEEE Conf. Antenna Meas. Appl. (CAMA)*, Guangzhou, China, Dec. 2022, pp. 1–3.

[41] M. -H. Chung, D. -H. Je, S. -T. Han, and S.-R. Kim, "Development of a 85 115 GHz 90-deg phase shifter using corrugated square waveguide," in *Proc. 44th Eur. Microw. Conf.*, Rome, Italy, Oct. 2014, pp. 1146–1149.

[42] A. Palomares-Caballero, A. Alex-Amor, P. Padilla, F. Luna, and J. Valenzuela-Valdes, "Compact and low-loss V-band waveguide phase shifter based on glide-symmetric pin configuration," *IEEE Access*, vol. 7, pp. 31297–31304, 2019.

[43] Z. Niu et al., "Mode analyzing method for fast design of branch waveguide coupler," *IEEE Trans. Microw. Theory Techn.*, vol. 67, no. 12, pp. 4733–4740, Dec. 2019.

[44] Z. Niu et al., "A 400 GHz broadband multi-branch waveguide coupler," in *Proc. UCMMT*, London, U.K., 2019, pp. 1–2.

[45] H. Riblet, "The short-slot hybrid junction," *Proc. IRE*, vol. 40, no. 2, pp. 180–184, Feb. 1952.

[46] K. Kuroiwa et al., "Short-slot hybrid coupler using linear taper in W-band," *J. Infr., Millim., Terahertz Waves*, vol. 34, no. 12, pp. 815–823, Oct. 2013.

[47] K. Lomakin et al., "3D printed E-band hybrid coupler," *IEEE Microwave Wireless Compon. Lett.*, vol. 29, no. 9, pp. 580–582, Sep. 2019.

[48] P.-H. Chiang, D.-B. Lin, H.-J. Li, and G. Stuber, "Joint estimation of carrier-frequency and sampling-frequency offsets for SC-FDE systems on multipath fading channels," *IEEE Trans. Commun.*, vol. 56, no. 8, pp. 1231–1235, Aug. 2008.

[49] *Digital Video Broadcasting (DVB); Second Generation Framing Structure, Channel Coding and Modulation Systems for Broadcasting, Interactive Services, News Gathering and Other Broadband Satellite Applications (DVB-S2)*, Standard ETSI EN 302 307, V1.2.1, Apr. 2009.

[50] Q. Wu, X. Jiang, and C. Zhang, "Attenuation of orbital angular momentum beam transmission with a parabolic antenna," *IEEE Antennas Wireless Propag. Lett.*, vol. 20, pp. 1849–1853, 2021.

[51] T. Nguyen, M. Hirabe, R. Zenkyu, M. Uchida, and E. Sasaki, "An experimental study on OAM mode-multiplexing with dielectric lens fed by uniform circular array," in *Proc. Int. Symp. Antennas Propag. (ISAP)*, Phuket, Thailand, Oct. 2017, pp. 1–2.

Hirofumi Sasaki (Member, IEEE) received the B.E. and M.E. degrees in engineering from Osaka University, Osaka, Japan, in 2011 and 2013, respectively. He joined the NTT Network Innovation Laboratories, Nippon Telegraph and Telephone Corporation (NTT), Japan, in 2013. Since 2015, he has been engaged in research on high-capacity wireless communications in millimeter-wave regions. His research interests include mm-Wave, THz, and optical communications, electromagnetic information theory, THz waveguide design, and digital signal processing for wireless communications. He received the Best Paper Award from the Institute of Electronics, Information and Communication Engineers (IEICE) SmartCom in 2016, the Best Paper Award and Special Technical Award in Smart Radio from the IEICE Smart Radio in 2017, and the IEICE Young Researcher's Award in 2017. He served as the Secretary for the IEEE GLOBECOM 2019 Workshop on High Capacity Point-to-Point Wireless Communications (HCPtP) and the IEEE GLOBECOM 2020, 2022, and 2023 Workshops on High Capacity Wireless Communications (HCWC).

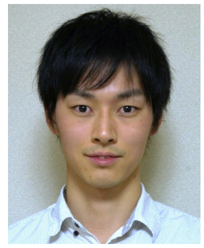

Yasunori Yagi (Member, IEEE) received the B.E. and M.E. degrees in electrical engineering from Tokyo University of Science, Tokyo, Japan, in 2015 and 2017, respectively. He joined the Wireless System Innovation Laboratory, NTT Network Innovation Laboratories, Nippon Telegraph and Telephone Corporation (NTT), in 2017. Since then, he has engaged in research on high-capacity and terahertz wireless communication. His research interests include wireless communications, microwave, millimeter-wave, terahertz-wave circuits, and digital signal processing. He received the Communication Express (ComEx) Best Letter Award from the Institute of Electronics, Information and Communication Engineers (IEICE) in 2022. He was the Secretary of the IEEE PIMRC 2022 Workshop on Electromagnetic Information Theory (EMIT 2022). He was the Technical Program Committee Member of the IEEE PIMRC 2023 Workshop on Electromagnetic Information Theory and IEEE VTC2023-Fall.

Riichi Kudo (Member, IEEE) received the B.S. and M.S. degrees in geophysics from Tohoku University, Japan, in 2001 and 2003, respectively, and the Ph.D. degree in informatics from Kyoto University in 2010. In 2003, he joined the NTT Network Innovation Laboratories, Japan. He was a Visiting Fellow with the Center for Communications Research (CCR), Bristol University, U.K., from 2012 to 2013, and NTT Docomo Inc., from 2015 to 2018. He has been with the NTT Network Innovation Laboratories since 2018. He is a member of IEICE. He received the Young Engineer Award from IEICE in 2006, the IEEE AP-S Japan Chapter Young Engineer Award in 2010, the Best Paper Award from IEICE in 2011 and 2016, and the Best Paper Award from IEICE Communications Society in 2017 and 2023.

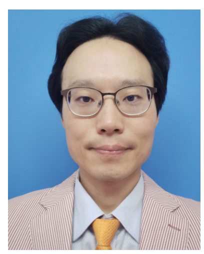

Doohwan Lee (Senior Member, IEEE) received the B.S. (Hons.) and M.S. degrees in electrical engineering from Seoul National University, South Korea, in 2004 and 2006, respectively, and the Ph.D. degree in electrical engineering and information systems from The University of Tokyo in 2009. He has been with the NTT Network Innovation Laboratories since 2009. From 2012 to 2014, he was a full-time Lecturer with the Research Center for Advanced Science and Technology, The University of Tokyo. From 2016 to 2018, he was a part-time Lecturer at Kanagawa University. His research interests include compressed sensing, software/cognitive radio, signal processing, OAM multiplexing, and multi-shape radio. He received the Best Paper Award and Best Technical Exhibition Award from the Institute of Electronics, Information and Communication Engineers (IEICE) Software Radio in 2011, the IEICE Communications Society Excellent Paper Award in 2012, the IEICE Short Range Wireless Communications (SRW) Young Researcher's Award in 2016, the Best Technical Exhibition Award from SmartCom in 2014, the Best Paper Award from SmartCom in 2016, the Best Paper Award and Special Technical Award in Smart Radio from IEICE Smart Radio in 2017, the Distinguished Contributions Award from IEICE Communications Society in 2021, and the ComEX Best Letter Award in 2023. He has served as the General Co-Chair for many workshops held at IEEE ICC, GLOBECOM, PIMRC, and VTC. He is the Co-Chair of the Membership Development Committee (MDC) of the IEEE ComSoC APB.